Heliyon 9 (2023) e21423

Contents lists available at ScienceDirect

Heliyon

journal homepage: www.cell.com/heliyon

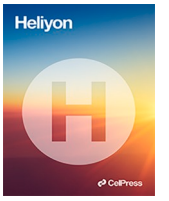

Photocatalytic degradation of tetracycline using surface defective black TiO_2–ZnO heterojunction photocatalyst under visible light

Lawrence Sawunyama [a], Opeyemi Oyewo [c], Damian C. Onwudiwe [a,b,*], Seshibe S. Makgato [c]

[a] *Material Science Innovation and Modelling (MaSIM) Research Focus Area, Faculty of Natural and Agricultural Sciences, North-West University, Mafikeng Campus, Private Bag X2046, Mmabatho, 2735, South Africa*
[b] *Department of Chemistry, School of Physical and Chemical Sciences, Faculty of Natural and Agricultural Sciences, North-West University, Mafikeng Campus, Private Bag X2046, Mmabatho 2735, South Africa*
[c] *Department of Chemical Engineering, College of Science, Engineering and Technology, University of South Africa, South Africa*

ARTICLE INFO

Keywords:
Metal oxides
Defect engineering
Oxygen vacancies
Heterojunction
Tetracycline

ABSTRACT

Fabrication of heterojunction and surface defective engineering, through the formation of oxygen vacancies, are among the various photocatalytic enhancement techniques. A combination of these techniques has the prospect of enhancing photocatalytic activities through improved light absorption capabilities and charge separation process of the photocatalysts. In this study, a heterojunction of black titanium oxide-zinc oxide ($BTiO_2$–ZnO) nanocomposite was synthesized using the conventional sol-gel approach, coupled with aluminum foil-assisted $NaBH_4$ reduction. The structure, morphology, surface properties, and optical characteristics of the synthesized material were studied using Fourier transform infrared spectroscopy (FTIR), X-ray diffraction (XRD), UV–vis absorption spectra, scanning electron microscope (SEM), Energy-dispersive X-ray spectroscopy (EDS), and transmission electron microscope (TEM). The XRD confirmed the successful formation of $BTiO_2$–ZnO heterostructure, while SEM revealed the structural morphology as pseudo-spherical with slight agglomeration. $BTiO_2$–ZnO was found to be more efficient than $BTiO_2$ and BZnO for the removal of tetracycline with degradation efficiencies of 63, 58, and 56 % respectively. The effects of process parameters such as the amount of photocatalyst, pollutant's concentration, and the initial solution pH on photocatalytic degradation study were systematically explored. The results confirm that the formation of the heterostructure from $BTiO_2$ and BZnO could offer a facile route to improving the catalytic degradation of tetracycline. Therefore, this study offers a novel perspective on the design of efficient metal oxide photocatalyst systems that rely on the integration of defect engineering and heterojunction for the removal of organic contaminants.

1. Introduction

The rising global population, increasing outbreaks of diseases, and high demand for food production have resulted in the increased usage of pharmaceutical products [1]. These include antibiotics, and among them, tetracycline is one of the most used. Its wide

* Corresponding author. Material Science Innovation and Modelling (MaSIM) Research Focus Area, Faculty of Natural and Agricultural Sciences, North-West University, Mafikeng Campus, Private Bag X2046, Mmabatho, 2735, South Africa.
E-mail address: Damian.Onwudiwe@nwu.ac.za (D.C. Onwudiwe).

https://doi.org/10.1016/j.heliyon.2023.e21423
Received 11 June 2023; Received in revised form 14 October 2023; Accepted 20 October 2023
Available online 30 October 2023

consumption compared to other antibiotics used by humans and animals is attributed to its benefit, for example, tetracycline improves the growth rate in aquaculture and poultry industries [2–4]. Despite its huge benefits, the discharge of tetracycline-contaminated effluents into the aquatic environment has given rise to persistent ecological contamination, antibiotic resistance, and eco-toxicological effects on plants and aquatic lives [5,6]. The consequence of these is the upsetting of the food chain. In humans, the effects of excess consumption of tetracycline include teeth staining, skin side effects, oesophagus damage, and gastrointestinal disturbances [7,8].

Generally, pharmaceutical contaminants in the environment are a challenge to manage because (1) conventional wastewater remediation methods are unable to remove them completely, (2) they have detrimental effects even at low concentrations, and (3) their rate of discharge into the environment exceeds their rates of degradation. This is because they are poorly absorbed by humans, livestock, and poultry; thus discharged as unmetabolized active substances, (4) most pharmaceutical pollutants such as unused drugs, expired drugs, agricultural and aquaculture pharmaceuticals can easily enter water bodies directly [9–11]. Therefore, it is important to devise some feasible, very effective, environmentally-friendly, and affordable methods that can mineralize tetracycline from wastewater to conserve water resources and achieve the sustainable development goal 6.

Several methods such as membrane technology [12,13], bioremediation [14], advanced oxidation processes (AOPs), electrocoagulation [15], adsorption [16], and hybrid techniques [17] have been used for the removal of pharmaceuticals from wastewaters. However, they all have different drawbacks and advantages. One of the most convenient methods for the complete removal of these pharmaceuticals is the advanced oxidation process, due to its high oxidation effectiveness and no generation of secondary pollutants. The advanced oxidation process is applicable in different processes including photocatalysis, photolysis, Fenton oxidation, electrochemical, ozone, and sonolysis [18]. Photocatalysis by metal oxide nanoparticles, zeolites, metal-organic frameworks, and nanorods has since attracted much interest due to their great potential to utilize the complete solar spectrum in photocatalytic reactions. Among them, metal oxide nanoparticles are one of the most efficient and effective AOP that is effective for the removal of tetracycline from wastewater. Examples of metal oxide nanoparticles that have been reported include ZnO, Fe_2O_3, TiO_2, CuO, MgO, SiO_2, and SnO_2. Out of the several metal oxides nanoparticles, ZnO and TiO_2 have been mostly reported due to their ease of synthesis, chemical stability, cost-effectiveness, long-standing photostability, non-corrosive property, and non-toxicity [19]. However, these nanomaterials utilize visible light inefficiently because of their wide band gap energies and fast recombination process of the photogenerated electron/hole pairs, which subsequently affects photocatalytic efficiency [20]. Therefore, several studies have been carried out to improve the photocatalytic efficiency of metal oxide nanoparticles such as ZnO and TiO_2 through the reduction of recombination rate and shifting of the optical response from UV to the visible spectral range because visible light accounts for 45 % of the solar energy [21]. These strategies include (1) heterojunction fabrications, (2) defect engineering, (3) doping with various elements and (4) co-catalyst loading [22,23]. Most published research papers on ZnO and TiO_2 technologies in recent years, focused on single photocatalytic enhancement technique. For example, Apostolescu et al. [23] studied the degradation of chlortetracycline and ceftriaxone using heterojunction of CeO_2/ZnO. The results showed an increase in the degradation efficiency of the antibiotics by the heterojunction system compared to the CeO_2 and ZnO tested separately. Andronic et al. [4] reported the synthesis of black TiO_2 with Ti^{3+} defects and oxygen vacancies via defect engineering. The synthesized nanomaterial exhibited very good photocatalytic degradation of organic pollutants compared to pristine TiO_2. However, very few studies reported the combination of photocatalytic enhancement techniques of both materials in single system. Therefore, in this current study, the formation of heterojunction of TiO_2 and ZnO nanoparticles together with the engineering of their surface defects have been synergistically employed to enhance the photocatalytic degradation of tetracycline (TC).

The surface defected heterostructure was obtained by the conventional sol-gel approach coupled with aluminium foil assisted $NaBH_4$ reduction. The performance of the Black ZnO, Black TiO_2, and Black TiO_2–ZnO samples was studied under direct light. The process variables such as the initial concentration of tetracycline and the catalyst loading were explored to establish the performance of the nanocomposite in the TC degradation process. The surface defected heterojunction photocatalytic nanomaterial is expected to have low bandgap energy and thus high degradation rate in direct sunlight. This study is relevant with respect to the development of enhanced novel photocatalysts for the degradation of antibiotics.

2. Experimental

2.1. Materials

Titanium tetra-isopropoxide [$Ti(OCH(CH_3)_2)_4$, 98 %], zinc acetate [$Zn(CH_3COO)_2{\cdot}2H_2O$, ≥98 %,], sodium hydroxide [NaOH, 98 %], absolute ethanol [CH_3CH_2OH, >99 %], sodium borohydride, [$NaBH_4$, >98 %], and hydrochloric acid [HCl, 28 %] were purchased from Merck, South Africa. All the chemicals were of analytical grade. The nanomaterials were prepared by following already reported procedures [24,25].

2.2. Synthesis of ZnO nanoparticles

A conventional sol-gel approach was used to synthesize ZnO nanoparticles from zinc acetate dihydrate and sodium hydroxide. Briefly, about 10 g of $Zn(CH_3COO)_2{\cdot}2H_2O$ was mixed with 200 mL of distilled water and stirred continuously for 20 min at 35 °C. Thereafter, 0.8 M NaOH was added in dropwise to the mixture to adjust the pH. The resultant mixture was then stirred for 2 h, giving rise to a white sol. After that the sol was aged for 24 h to convert it to a white gel, which was centrifuged, and then washed several times with distilled water. The obtained powder was dried for 12 h at 150 °C and finally calcined at 400 °C in the muffle furnace for 3 h.

2.3. Synthesis of TiO_2 nanoparticles

A conventional sol-gel approach was used to synthesize TiO_2 nanoparticles from titanium tetra-isopropoxide and absolute ethanol. About 30 mL of [$Ti(OCH(CH_3)_2)_4$, 98 %] was mixed with 75 mL of CH_3CH_2OH and stirred well for 45 min. Then, 30 mL of distilled water was introduced in dropwise to initiate the ionization process. The resultant mixture was stirred for 45 min, to afford a white sol, which was aged for 24 h to form a white gel. The gel product was centrifuged and washed several times with distilled water. The obtained powder was dried for 12 h at 150 °C and finally calcined at 500 °C in the muffle furnace for 3 h.

2.4. Synthesis of TiO_2–ZnO heterojunction nanoparticles

The synthesized ZnO and TiO_2 sol were mixed and thoroughly stirred on a magnetic stirrer plate for 4 h at 25 °C. The formed TiO_2–ZnO precipitate was aged for 24 h, then centrifuged and washed with distilled water. The obtained powder was dried for 12 h at 150 °C and followed by calcination at 500 °C for 3 h.

2.5. Synthesis of $BTiO_2$, BZnO and $BTiO_2$–ZnO nanoparticles

Firstly, 2 g of each as-prepared material (pristine ZnO, pristine TiO_2 and TiO_2–ZnO nanoparticles) was mixed with about 0.4 g of $NaBH_4$ powder, and the mixture was tightly wrapped in an aluminium foil. The resultant aluminium foils were calcined in a muffle furnace at three different temperatures of 300, 350 and 400 °C for 1 h. The enclosed samples were cooled down to room temperature, washed with methanol, and several times with deionized water to remove any sodium and borate impurities. The washed samples were then dried at 100 °C overnight.

2.6. Characterization of synthesized nanocomposites

Functional groups of the synthesized materials were analysed on a Bruker alpha-P FTIR spectrophotometer. The XRD analysis was carried out on a Bruker D8 Advance X-ray diffractometer (Karlsruhe, Germany). The diffractometer has single-wavelength Cu Kα radiation (λ = 1.546060 Å). JEOL 2100 JEM Transmission electron microscopy (TEM) was used to evaluate the surface morphology of the synthesized materials. Surface morphology, composition, and sizes of the nanoparticles were evaluated using a Quanta FEG 250 Environmental scanning electron microscope (ESEM) coupled with EDX. PerkinElmer λ20 UV–vis spectrophotometer was used to obtain the absorption spectra, and Malvern Zetasizer Nanoseries was used for the measurement of the Zeta potential.

2.7. Photocatalytic degradation of tetracycline in water

The photocatalytic performance of the synthesized materials was evaluated on the degradation of tetracycline in water. The

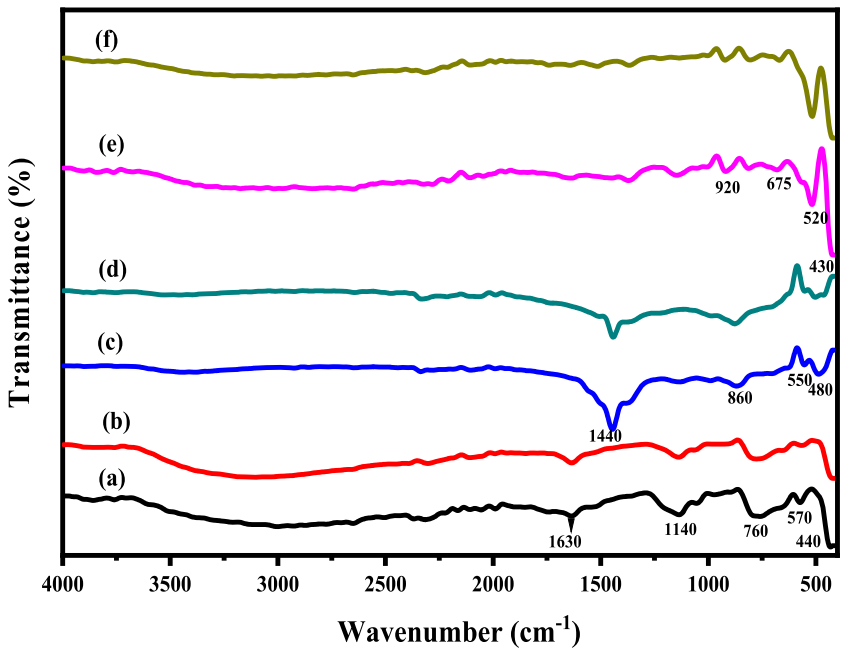

Fig. 1. FTIR spectra of (a) pristine TiO_2, (b) $BTiO_2$, (c) pristine ZnO, (d) BZnO, (e) TiO_2–ZnO, and (f) $BTiO_2$–ZnO.

photocatalyst was first submerged in a photocatalytic reactor system kept at a constant temperature of 25 °C. A 250 mL tetracycline solution with a starting concentration of 50 mg/L was placed in the reactor system. The system was agitated for 30 min in complete darkness, to achieve steady-state adsorption-desorption equilibrium. The suspension was continuously stirred while exposed to 300 W of Xe lamp light. At intervals of 20 min, 5 mL of aliquots were taken from the suspension and immediately filtered through a 0.22 μm microporous membrane to obtain the solutions. TC degradation was measured at 200–900 nm wavelength using a UV–visible spectrophotometer. The effect of process variables such photocatalyst loading, tetracycline concentration, and pH were assessed. The percentage of tetracycline that has been photocatalytically degraded was obtained by using Equation (1).

$$\text{Percentage removal of Tetracycline} = \frac{Co - C}{Co} * 100 \quad (1)$$

Where C_o is the concentration of tetracycline before photocatalysis and C is the concentration of tetracycline after the photocatalytic process.

3. Results and discussion

3.1. Fourier transforms infra-red (FT-IR) spectroscopy

Infra-red spectra of the pristine TiO_2, $BTiO_2$, pristine ZnO, BZnO, TiO_2–ZnO and $BTiO_2$–ZnO are presented in Fig. 1 (a -f) respectively. The spectrum of pristine TiO_2 and $BTiO_2$ showed all the characteristic bands of TiO_2, with the vibrational bands of Ti–O observed around 470 and 590 cm^{-1} [26,27]. The peak observed at 1630 cm^{-1} corresponds to the deformative vibration of Ti–OH stretching mode [28,29]. The peak at 760 cm^{-1} is related to Ti–O stretching band, which is the characteristic peak of TiO_2 [30,31]. FTIR spectra of the pristine ZnO and BZnO nanoparticles display vibrational bands attributed to the Zn–O vibrations of ZnO around 400–600 cm^{-1} [32]. A band at 860 cm^{-1} could be ascribed to the stretching vibration of the Zn–O bond [33]. A band at 860 cm^{-1} could be ascribed to the stretching vibration of the Zn–O bond [33]. The bands at 1440 cm^{-1} could be assigned to the asymmetric stretching modes of oxygen molecules present in the sample [34,35]. The spectra of TiO_2–ZnO and $BTiO_2$–ZnO composites showed bands that are consistent with pristine TiO_2 and ZnO nanoparticles. The absorption peak at 675 cm^{-1} is due to the vibrational mode of −Zn–O–Ti group [36]. During the compositing reaction, the interaction between these two metal oxides (TiO_2 and ZnO) broke the metal-oxygen bonds, facilitating the compositing of the complex metal oxides system that resulted in the desired TiO_2–ZnO and black TiO_2–ZnO. In the composite, the disappearance of peaks at 1630 cm^{-1} and 1440 cm^{-1} due to Ti-OH and symmetric stretching modes of the oxygen (O_2) molecules that were initially present in the pristine TiO_2 and ZnO respectively further supports the successful formation of the heterojunction materials.

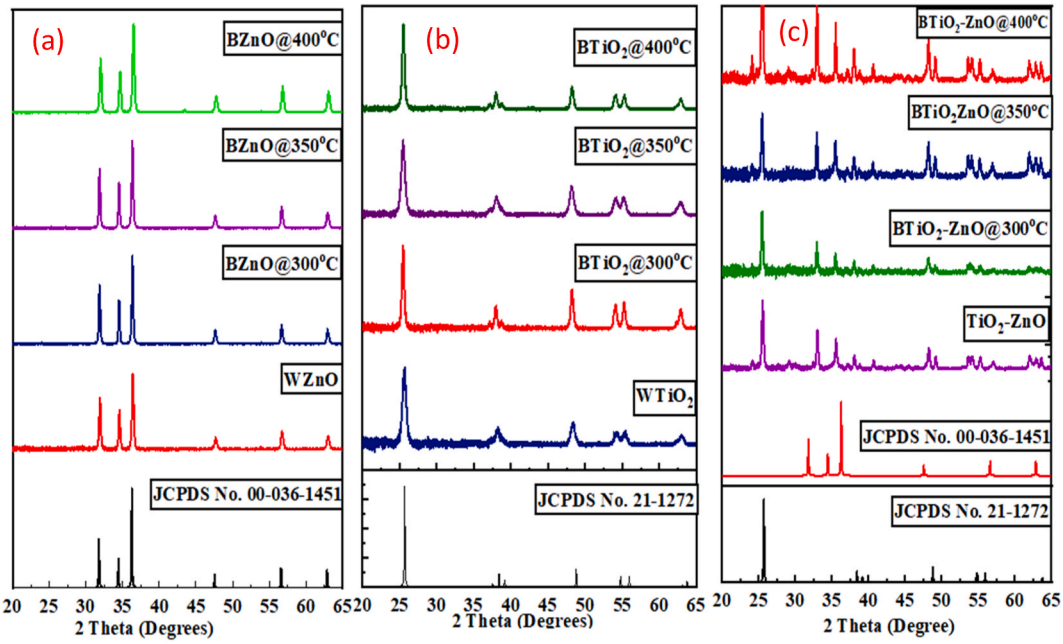

Fig. 2. X-ray diffraction patterns of (a) overlaid pristine ZnO and BZnO synthesized at 300 °C, 350 °C and 400 °C, (b) overlaid pristine TiO_2 and $BTiO_2$ synthesized at 300 °C, 350 °C and 400 °C, and (c) TiO_2–ZnO and $BTiO_2$–ZnO synthesized at 300 °C, 350 °C and 400 °C.

3.2. X-ray diffraction (XRD) analysis

XRD analysis was used to investigate the crystal structure and phase purity of the synthesized materials. Fig. 2 presents the X-ray diffraction spectra of pristine ZnO together with BZnO synthesized at 300 °C, 350 °C and 400 °C (Fig. 2a), pristine TiO_2 and $BTiO_2$, synthesized at 300 °C, 350 °C and 400 °C (Fig. 2b), and TiO_2–ZnO and $BTiO_2$–ZnO synthesized at 300 °C, 350 °C and 400 °C (Fig. 2c). The diffraction patterns of the pristine ZnO and BZnO at different temperatures displayed six characteristics peaks of hexagonal wurtzite phase (JCPDS no 036–1451) at 2 theta values of 31.5, 34.1, 36.1, 56.6 and 64.0° which can be indexed to the (100), (002), (101), (102), (110) and (200) planes respectively [34]. This, thus, indicates that the pristine ZnO has the same crystal structure as BZnO, which suggest that the surface defective engineering does not affect the crystal structure but only altered the colour of pristine ZnO to black. The diffraction peaks for major anatase phase peaks are reported to appear at 25.4, 37.7, 47.8, and 54.8°, while the weaker rutile phases are located at 27.4 and 36°. The diffraction pattern of the pristine TiO_2 and $BTiO_2$ synthesized at different temperatures confirmed the presence of only the anatase phase with (JCPDS Card no. 21–1272) (Fig. 2b). The reflection at 2θ angle of 25.6, 37.9,48, 53.9, and 55.2° correspond to the (1 0 1), (0 0 4), (2 0 0), (1 0 5), and (2 1 1) planes respectively [37,38]. The XRD patterns of the heterojunctions system are composed of TiO_2 (anatase) and ZnO (hexagonal) peaks at (25.6, 37.9,48, 53.9, and 55.2°) and (31.5, 34.1, 36.1, 56.6 and 64°) respectively, indicating that the introduction of surface defects did not alter the crystallographic structure. The most common possible defects that might have developed when TiO_2 and ZnO were reduced by $NaBH_4$ for 1 h at 350 °C are oxygen vacancies. There is also a noticeable slight increase in the peak intensities as reaction temperature increased, which proved that the induced oxygen vacancies and Ti^{3+} resulted to increased crystallinity in the synthesized composites.

Debye-Scherrer (equation (2)) and Lattice micro strain (equation (3)) were used to calculate the crystalline size and lattice micro strain [39] of each of the synthesized catalysts and the values are presented in Table 1. As the temperature increased, the crystallite size of each synthesized material marginally increased. Compared to other synthesized materials, $BTiO_2$–ZnO has the largest lattice micro strain, which could enhance the photocatalytic performance of the composite relative to the individual metal oxide since more hydroxyl radicals would be generated due to higher possibility of photocarrier transition and hole trapping [40,41]. The dislocation density (δ) of the synthesized materials was calculated from the average particle size values (equation (4)), [42]. The sample with the lowest dislocation density was $BTiO_2$–ZnO produced at 350 °C (Table 1). The lowest dislocation density value indicates that the $BTiO_2$–ZnO produced at 350 °C possess a high degree of crystallinity compared to other synthesized materials [43].

Debye–Scherrer formulae:

$$D = K\lambda/\beta \mathrm{Cos}\ \theta \tag{2}$$

Where D = Crystallites size (nm), K = Scherrer's constant (Shape factor) (Here, taken as 0.94), λ = Wavelength of X-rays (Å), β = F. W. H. M (Full Width at Half Maxima in degrees), θ = Peak position in XRD graph (that is 2θ in degrees).

$$\textit{Lattice strain}\ (\varepsilon) = \frac{\beta\ Cos\ \theta}{4} \tag{3}$$

$$\text{Dislocation density}\ \delta = \frac{1}{D^2} \tag{4}$$

3.3. Optical properties of the binary metal oxides and composite oxides

UV–vis spectrometer was used to determine the optical properties of the synthesized materials by measuring the absorbance. Fig. 3a–c presented the UV-absorption spectra of (a) pristine ZnO together with BZnO, (b) pristine TiO_2 and $BTiO_2$, and (c) TiO_2–ZnO and $BTiO_2$–ZnO synthesized at 300, 350. And 400 °C respectively. The absorption spectra of the pristine ZnO and BZnO synthesized at 300 and 350 °C exhibited a narrow peak in the UV region around 380 nm (Fig. 3a). BZnO synthesized at 400 °C showed a peak near the band edge region (at about 400 nm) with a dramatic increase in the absorption intensity. Pristine TiO_2 and $BTiO_2$ (Fig. 3b) also showed in the near-UV region with absorption edge at around 400 and 425 nm respectively. $BTiO_2$ synthesized at 350 and 400 °C absorbed in

Table 1
Crystallite size and lattice microstrain of synthesized materials.

Synthesized nanomaterial	Crystallite size (nm)	Lattice strain	Dislocation density (δ) (m^2)
Pristine ZnO	26.15	6.64×10^{-2}	1.46×10^{-3}
BZnO@300 °C	28.61	5.59×10^{-2}	1.22×10^{-3}
BZnO@350 °C	31.47	5.08×10^{-2}	1.01×10^{-3}
BZnO@400 °C	34.61	6.72×10^{-3}	8.34×10^{-4}
Pristine TiO_2	13.86	1.68×10^{-3}	5.21×10^{-3}
$BTiO_2$@300 °C	13.41	1.73×10^{-3}	5.56×10^{-3}
$BTiO_2$@350 °C	20.46	7.27×10^{-3}	2.39×10^{-3}
$BTiO_2$@400 °C	21.20	8.12×10^{-3}	2.22×10^{-3}
TiO_2–ZnO	28.29	5.79×10^{-3}	1.25×10^{-3}
TiO_2–ZnO@300 °C	31.55	1.521×10^{-2}	1.00×10^{-3}
TiO_2–ZnO@350 °C	32.68	1.503×10^{-2}	9.36×10^{-4}
TiO_2–ZnO@400 °C	37.81	1.32×10^{-3}	6.99×10^{-4}

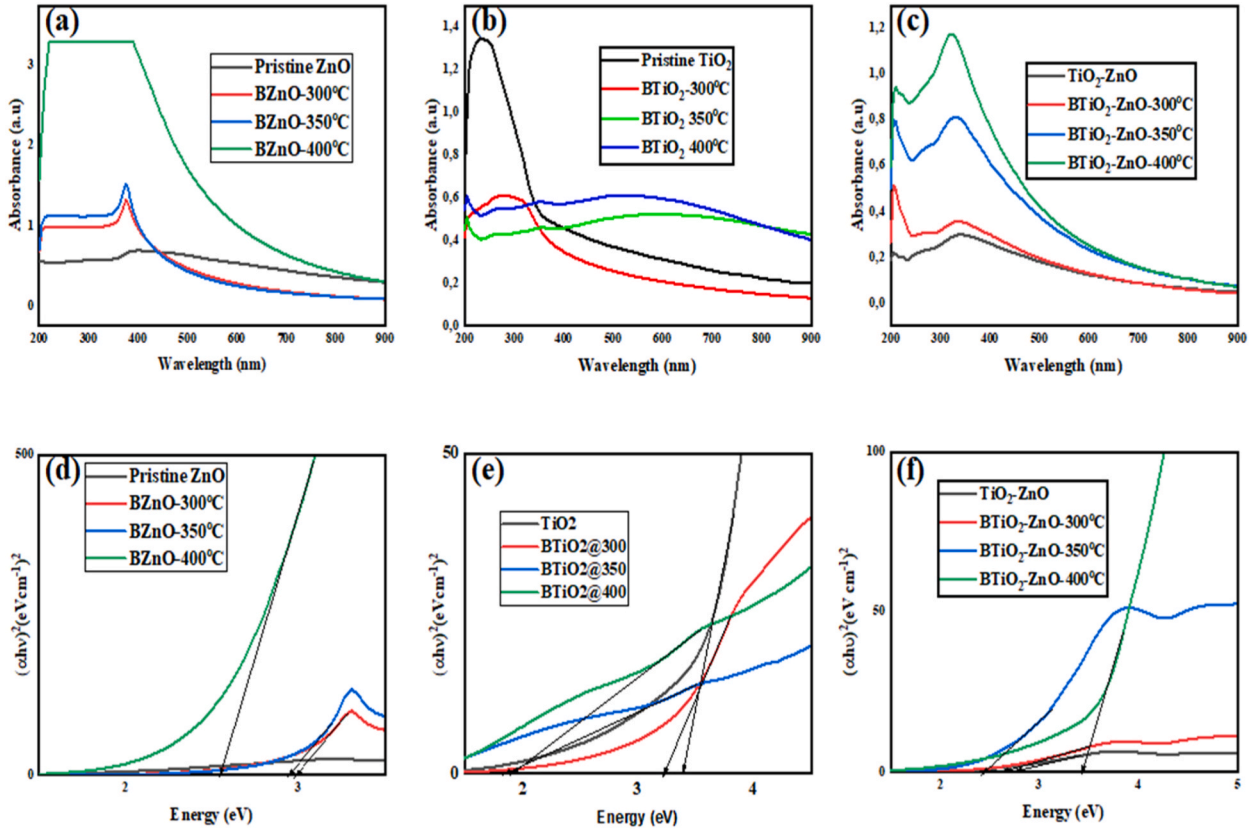

Fig. 3. Optical spectra of overlapped (a) ZnO and BZnO synthesized at 300 °C, 350 °C and 400 °C, (b) pristine TiO_2 and $BTiO_2$, synthesized at 300 °C, 350 °C and 400 °C, and (c) TiO_2–ZnO and $BTiO_2$–ZnO synthesized at 300 °C, 350 °C and 400 °C while d, e and f are the tauc plots respectively.

the near-UV to the visible region. The significant absorption of UV light was caused by the charge transfer from the 2p orbital of TiO_2 to 3 d orbital of the Ti^{4+} which acts as the valence band and conduction band respectively [44]. The spectrum of the heterojunction materials in Fig. 3c showed that the absorption edge was red-shifted relevant to the position of absorption in the pristine ZnO and pristine TiO_2; hence, confirmed that the absorption edge of both ZnO and TiO_2 can be changed through the formation of a heterojunction. The absorption intensities significantly increased as the reduction temperature increased during the defective engineering, and a slight shift in the optical absorption edge towards the longer wavelength region occurred. This may be ascribed to an increase in particle size and the nano-confinement effect of oxygen vacancies, which changed the local electronic states [45–47]. The optical bandgap energies-of the materials were obtained using Tauc plots of $(hv)^{1/2}$ against Eg and are shown in Fig. 3d–f. The optical bandgap energy became narrowed with the formation of oxygen vacancy in the heterojunction systems at different synthesis temperatures. The differences in band gap energy for the samples could be attributed to the formation of new electronic levels in the heterojunction. Therefore, more charge separation and increased lifetime of charge carriers in the material can be achieved [47,48]. Additionally, Equations (5) and (6) were used to calculate the conduction band potential (E_{CB}) and valence band potential (E_{VB}) of the composite nanomaterials.

$$E_{VB} = \chi - E_e - 0.5E_g \quad (5)$$

$$E_{CB} = E_{VB} - E_g \quad (6)$$

Table 2
Mulliken's electronegativity (χ), band gap energy (E_g), valence band (E_{VB}) and conduction band (E_{CB}) for the pristine nanoparticles and the nanocomposite.

Semiconductors utilized in photocatalytic studies.	χ (eV)	E_g (eV)	E_{CB} (eV)	E_{VB} (eV)
$BTiO_2$	5.82	1.8	0.42	+1.38
BZnO	5.78	3.8	−0.62	+4.42
$BTiO_2$–ZnO	5.82	2.5	0.07	−0.47

where Eg denotes the semiconductor's band gap energy, E_{VB} denotes the VB edge, E_{CB} denotes the CB edge, χ denotes the electronegativity of the semiconductor nanoparticles, and E_e denotes the energy of free electrons as measured on the hydrogen scale (4.5 eV). The values are 5.78 and 5.82 eV, respectively, for ZnO and TiO_2. Table 2 displays the calculated band alignments.

3.4. Morphological study

3.4.1. Scanning electron microscope (SEM) analysis

The surface morphologies of the synthesized materials were investigated and presented in Fig. 4a–f. The SEM micrographs of BZnO nanoparticles displayed small crystals with pseudo-spherical morphology aggregated on the surface. The micrograph of $BTiO_2$ nanoparticles, synthesized at 350 °C (presented in Fig. 3b) shows small spherical particles that formed into larger agglomerates. However, the $BTiO_2$–ZnO nanocomposite at different temperatures exhibited minimal agglomeration with a spherical shape. An increase in the synthesis temperature influenced both the size and shape of the nanocomposite (Fig. 3f). This increased the surface area of the nanocomposite, which could enhance the photocatalytic activities of these materials.

3.4.2. Transmission electron microscope (TEM), elemental mapping, and energy dispersive X-ray (EDX) analysis

Fig. S1 (a and b) show the TEM images and particle size histogram of BZnO nanoparticles respectively. The TEM images confirm that the nanomaterials are of spherical morphology which are visibly arranged in a chain-like configuration. The average particle size of the synthesized material was about 44.6 nm, which was close to the value obtained from the XRD pattern. The EDX spectrum of BZnO (Fig. S1c) shows the presence of only zinc and oxygen, and the even distribution of both elements (zinc and oxygen) within the modified binary metal oxide was confirmed by the elemental mapping images of Fig S1 (d-f).

The TEM images of $BTiO_2$ nanoparticles and the particle size distribution histogram are presented in (Figs. S2a and b) respectively. The nanoparticles were of spherical morphology with slight agglomeration, and the average particle size was about 15.0 nm and agrees with the crystalline size obtained from the XRD pattern. The representative EDX spectrum presented in Fig. 6c shows the distinct peaks corresponding to titanium and oxygen. The elemental mapping images in Fig. S2 e and f show that titanium and oxygen were homogeneously distributed across the $BTiO_2$ particles, suggesting a good dispersion of the elemental composition of the nanostructures.

A heterojunction of two binary components prepared via calcination process often have a high tendency to agglomerate. Figs (S3a and S4a) and Figs (5a and 6a) show the TEM, EDX and elemental mapping images for the heterojunction compounds TiO_2–ZnO, $BTiO_2$–ZnO (300 °C), $BTiO_2$–ZnO (350 °C), and $BTiO_2$–ZnO (400 °C) respectively. All the TEM images show highly agglomerated spherical nanograins. TEM images for $BTiO_2$–ZnO synthesized at 350 °C showed the least agglomeration indicating that it could be the best catalyst since agglomeration influences the optical properties of materials and therefore their ability to absorb and scatter the incoming radiation thereby influencing the photocatalytic activity [49]. The elemental composition of the nanocomposite is shown in the EDX spectrum presented in Figs (S3b and S4b) and Figs (5b and 6b) confirms heterojunctions are primarily composed of titanium, zinc and oxygen with no impurity. The elemental mapping images of the composite prepared at 350 °C (Fig. 5c–f) and at 400 °C

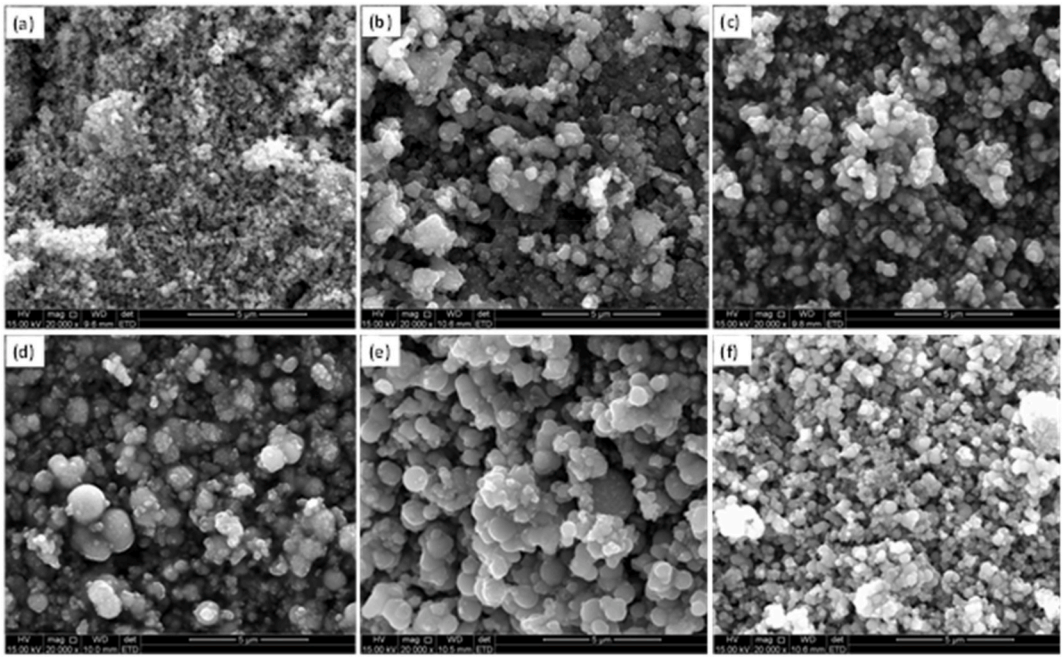

Fig. 4. SEM micrographs of (a) $BTiO_2$, (b) BZnO, (c) TiO_2–ZnO, (d) $BtiO_2$-ZnO synthesized at 300 °C, (e) $BTiO_2$–ZnO synthesized at 350 °C, and (f) $BTiO_2$–ZnO synthesized at 400 °C.

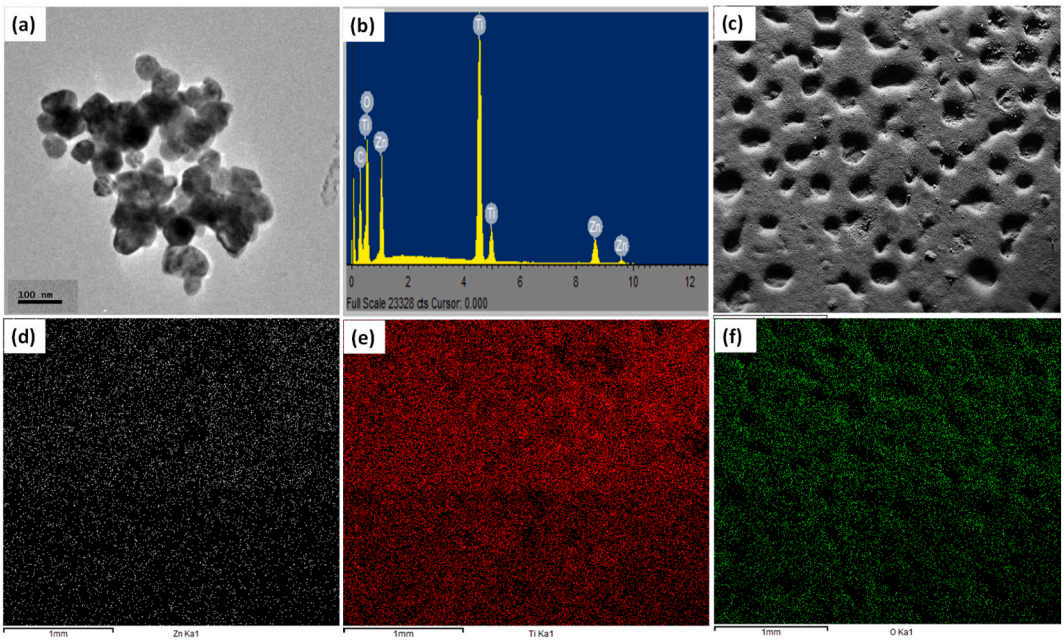

Fig. 5. (a) TEM image, (b) EDX spectra, (c) elemental mapping showing (d) Zn, (e)Ti, and (f) O elements of Black TiO_2–ZnO prepared at 350 °C for 1 h.

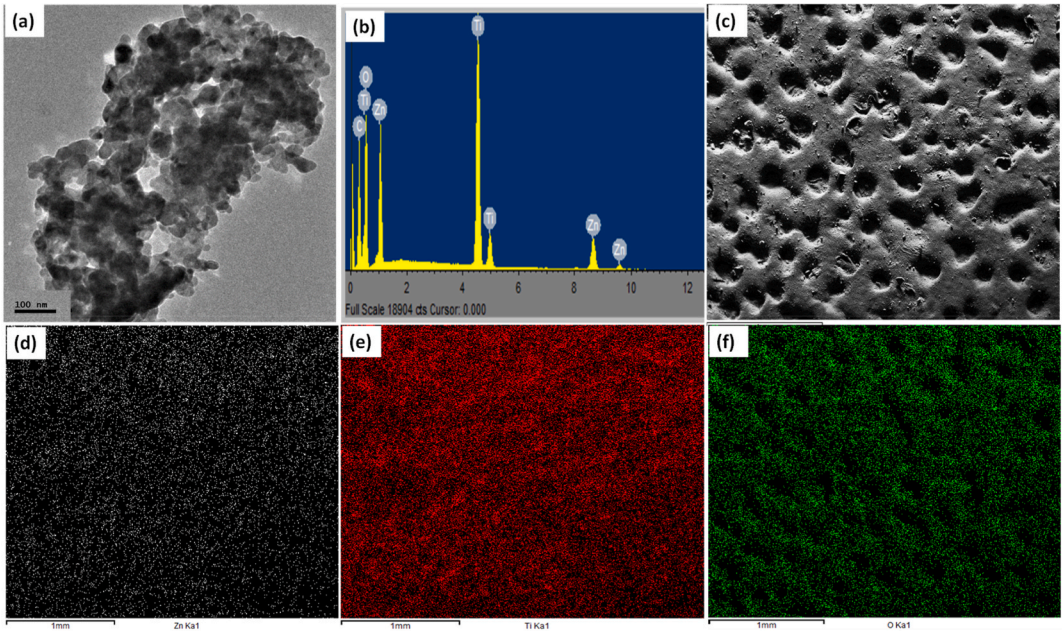

Fig. 6. TEM image, (b) EDX spectra, (c) elemental mapping showing (d) Zn, (e)Ti, and (f) O elements of Black TiO_2–ZnO prepared at 400 °C for 1 h.

(Fig. 6c–f) confirmed the uniform distribution of the titanium, zinc, and oxygen across the synthesized heterojunctions.

3.5. Photoluminescence (PL) study

The PL spectra of $BTiO_2$, BZnO, TiO_2–ZnO, and $BTiO_2$–ZnO with excitation wavelength of 325 nm are shown in Fig. 7. The observed peak, exhibited by all samples around 360 nm, is due to photoinduced charges naturally recombining from the conduction band to the valence band [50]. The observed lower PL emission intensity of the $BTiO_2$–ZnO heterojunction composite is related to the improvement of the charge separation rate, which in turn reduces the radiative recombination of electron-hole pairs. Efficient charge

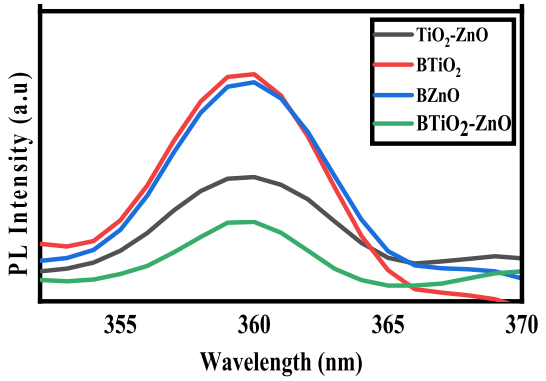

Fig. 7. Photoluminescence spectra of $BTiO_2$, BZnO, TiO_2–ZnO and $BTiO_2$–ZnO.

separation, therefore, increases the lifetime of the charge carriers and subsequently enhances the photocatalytic activity of the synthesized nanomaterial.

3.6. Photodegradation of tetracycline

The photocatalytic efficiency of the nanocomposites prepared at different temperatures (300, 350, and 400 °C) was evaluated on a 50 mg/L tetracycline concentration, 100 mg of each catalyst, and a pH of 5.6. The degradation patterns at various reduction temperatures, presented in Figs. S5a–c, were slightly different. Results of the preliminary study showed that the photocatalytic degradation efficiency of $BTiO_2$–ZnO at 350 °C was higher than in other nanocomposites. The smaller band gap energy of $BTiO_2$–ZnO (350 °C) might be responsible for the enhanced performance achieved. Therefore, the $BTiO_2$–ZnO at 350 °C was chosen for the subsequent evaluation of the photocatalytic degradation of TC in this study.

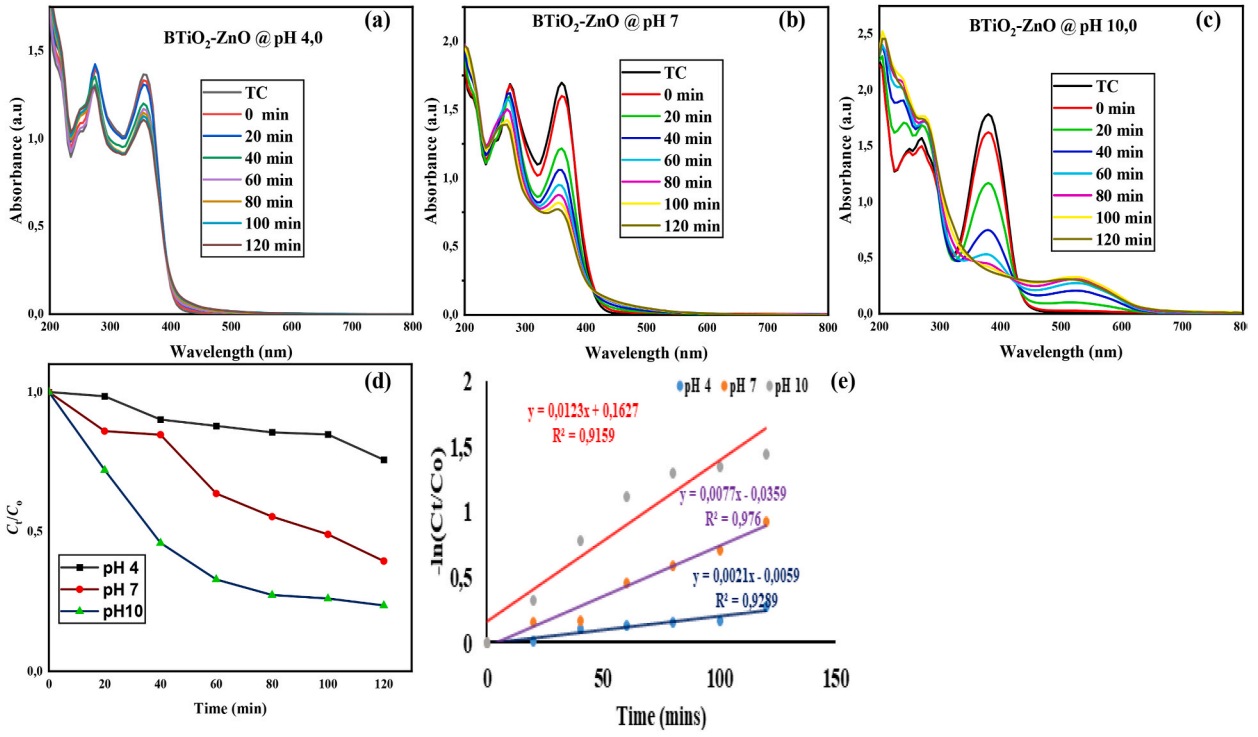

Fig. 8. Absorption spectra of TC (50 mg/L) at different time using 100 mg/L of $BTiO_2$–ZnO at pH values of (a) pH 4, (b) pH 7 and (c) pH 10, (d) rate of decomposition, and (e) the kinetics graph of the decomposition process.

3.7. Influence of TC solution pH on the degradation efficiency

Solution pH is an important factor in the evaluation of photocatalytic degradation of tetracycline because pH affects the electrical charge properties of the photocatalyst's surface. The pH determines the ionization state of the photocatalyst surface, and then affects the adsorption and photocatalytic performance of any photocatalyst [51,52]. The photocatalytic degradation efficiencies of TC in the pH range of 4, 7 and 10 were evaluated using 50 mg/L tetracycline concentration and 100 mg of each catalyst and presented in Fig. 8a, b, and c respectively. The photocatalytic degradation efficiencies of TC at different pH values followed the order of pH10 > pH7 > pH4. The results showed a similar trend with previously reported results [53], whereby the degradation of tetracycline in aqueous solution by nanosized TiO_2 was studied. The slow degradation of TC under acidic conditions may be because ZnO, which is one of the component compounds, is not acid resistant. It can also be attributed to the repulsive force between protonated TC and the positively charged catalyst. Aggregation of nanoparticles under acidic conditions is reported to contribute to poor photocatalytic activity of some metal oxide nanoparticles due to the reduced surface area of the photocatalysts [54]. The faster degradation of TC at pH 10 may be due to the alkaline pH, and hydroxyl radicals were easier to form by the oxidization of more hydroxide ions available on the photocatalyst surface. Fig. 8c shows that as the photocatalytic degradation of TC progresses under alkaline pH, the maximum absorption peak at 350 nm gradually decreases, while the minimum absorption peak at 276 nm slightly increased. Hence, confirms the increase in the concentration of the absorbing species at 276 nm. A new absorption peak appears at 550 nm which reveals the formation of by-products. Similar results on the emergence of new absorption peak under alkaline pH were previously reported [55]. The existence of by-products may be caused by the electrophilic attack on the TC ring structures that possess high electronic densities, such as aromatic rings and the keto-enol groups. Additionally, electronic density would alter the bond orbital energy of molecules, resulting in various rates of light absorption [56]. Fig. 8d and e shows the rate of decomposition and the kinetics graph of the decomposition process respectively.

The zeta potential of the synthesized materials was found to be +26.1, −45.1, and −39.5 ± 5.64 mV for BZnO, $BTiO_2$ and $BTiO_2$–ZnO Figs. S6a–c. The nanomaterials ($BTiO_2$–ZnO and $BTiO_2$) have negative zeta potential, which indicates strong stability and low agglomeration of the nanoparticles in solution because of stronger repelling forces [57–59]. Since both $BTiO_2$ and $BTiO_2$–ZnO have significantly charged surfaces, as shown by zeta potential studies, electrostatic interaction is unlikely to have an impact on tetracycline sorption on either material. This is because TC is an amphoteric molecule due to the presence of dimethylammonium, phenolic

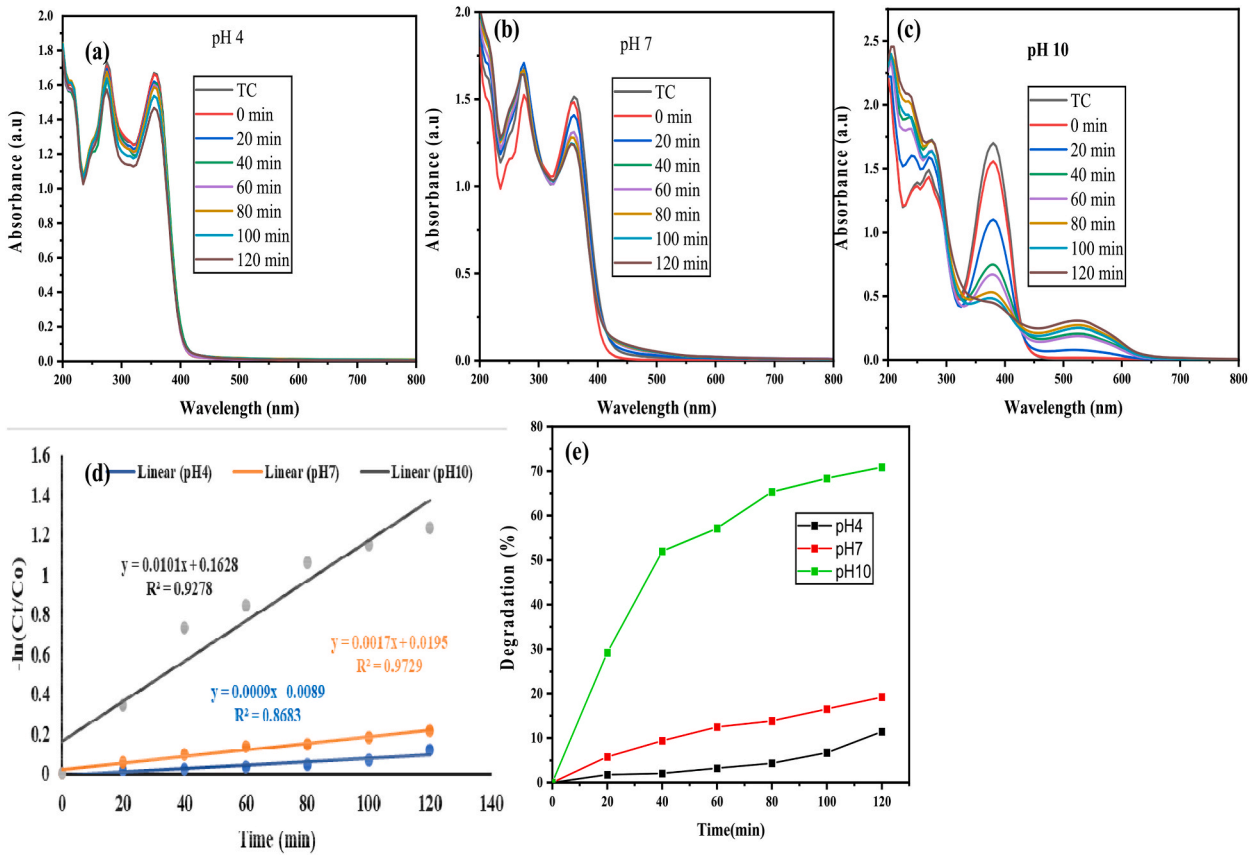

Fig. 9. Absorption spectra of TC showing its photolysis at different pH (a) 4, (b) 7, (c) 10, (d) Kinetic graphs at different pH values, and (e) percentage degradation of TC under visible light (TC initial concentration: 50 mg/L, catalyst dosage 100 mg/L).

diketone moiety and the tricarbonyl system. As a result, at pH values of >3, 3.3–7.7, and <7.7, TC occurs as cationic, zwitterionic, and anionic species, respectively [60].

The zeta potential was also established for pH values of 4, 7, and 10 (Fig. S6d) to assess the surface charges of $BTiO_2$–ZnO related to changes in pH. According to reported studies, neutral nanoparticles are those with a zeta potential between −10 and + 10 mV, whereas strongly cationic and strongly anionic nanoparticles are those with a zeta potential of greater than +30 mV and less than −30 mV, respectively [61]. Thus, net surface charge of the $BTiO_2$–ZnO nanocomposite is highly negative under pH 10 and pH 7 and was expected to repel the anionic form of the TC molecule and form strong electrostatic interactions with the cationic form of TC [62].

The photolysis of TC at different pH values of 4, 7 and 10 are shown in Fig. 9a, b and c respectively. The results show a favourable photolysis of tetracycline at pH 10, which may contribute to the increased photocatalytic degradation of the TC by $BTiO_2$–ZnO at pH 10. Lower photolysis of TC at pH 4 and pH 7 indicates poor degradation of TC^+ and TC°, respectively. The attraction between TC^- and hydroxyl radicles caused by the high electronic density of the TC^- ring system could be responsible for the high photolysis rate at pH 10 [63]. Since the bond orbital energy changes at high pH, TC tends to absorb more photons thereby enhancing photolysis [56]. Other studies has reported that tetracycline shows a favourable photolysis at alkaline pH [64]. A kinetics graph at different pH values, and percentage degradation of TC under visible light using an initial concentration of 50 mg/L and 100 mg/L catalyst dosage are shown in Fig. 9d and e respectively.

3.8. Influence of photocatalysts dose

The influence of photocatalyst dosage on the degradation of TC was evaluated in the absence of the photocatalyst (Fig. 10a) and using 75, 100 and 125 mg/L of $BTiO_2$–ZnO at a constant TC concentration of 50 mg/L, while a constant pH of 7 was maintained and the reaction was monitored for 120 min (Fig. 10b, c and d respectively). Photocatalytic degradation efficiency of TC was observed to increase as the catalyst dosage increases (Fig. 10e). The kinetics graphs of the decomposition process at initial TC concentration of 50 mg/L and solution pH 7 is presented in Fig. 10 f. This could be attributed to an increase in the number of active sites on the surface of the photocatalysts, which subsequently increased the production of hydroxyl radicals responsible for photocatalysis process [65]. Studies have shown that increase in the concentrations of catalyst has a direct effect on the photocatalytic activity, but only up to a certain level. This is because at a high catalyst loading, most of the catalysts may experience deactivation due to agglomeration and precipitation. This might reduce the amount of catalyst surface that is available for light absorption and, as a result, decreases the rate of pollutant degradation [66]. The marginal degradation of TC in the absence of the photocatalyst could be attributed to photolysis.

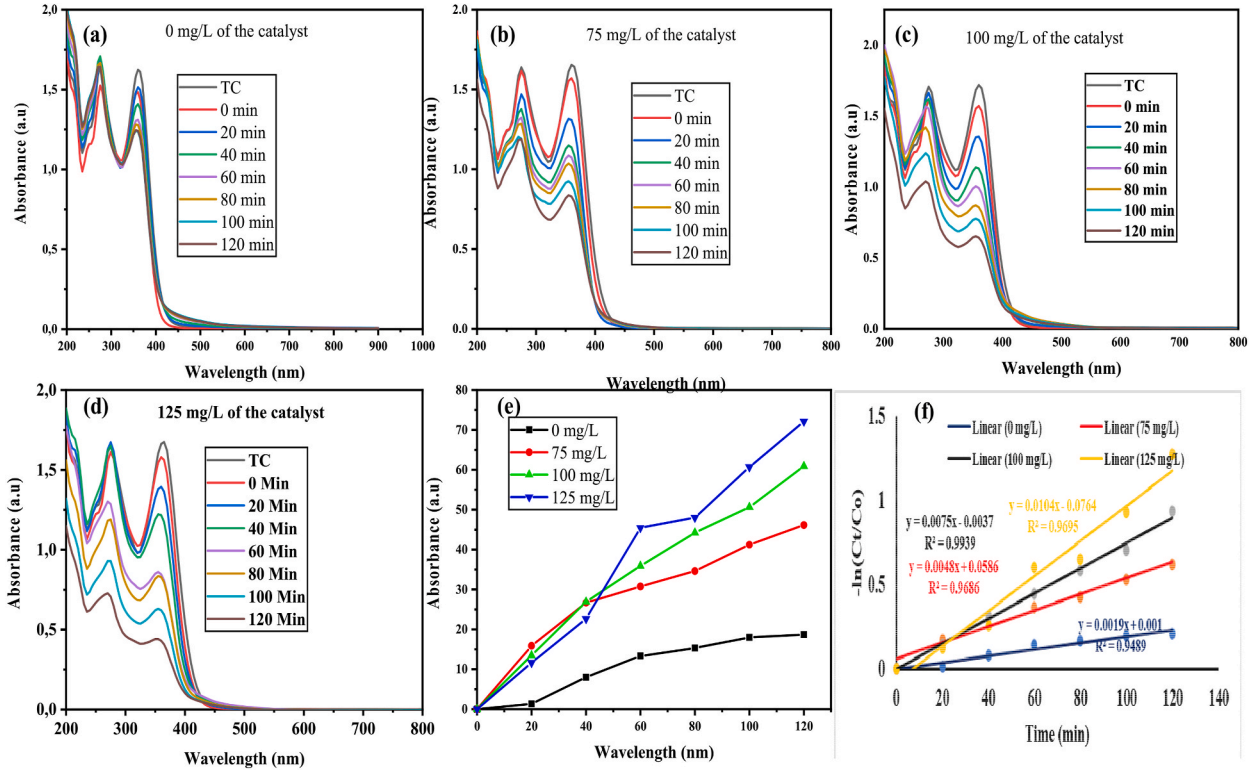

Fig. 10. Absorption spectra of TC showing its photodegradation by $BTiO_2$–ZnO nanocomposite at catalyst loading concentrations of (a) 0, (b) 75, (c) 100, and (d) 125 mg/L, and (e) percentage degradation of TC under visible light (TC initial concentration: 50 mg/L, pH: 7), and (f) kinetics of graphs of the decomposition process.

3.9. Influence of initial concentration of tetracycline on the degradation process

The influence of TC concentration on the degradation process was evaluated by using 100 mg of $BTiO_2$–ZnO to 1 L of 25–75 mg/L TC solution while maintaining a constant pH of 7 and the duration of the reaction was 120 min. The result of the degradation process is presented in Fig. 11(a–c). The photocatalytic degradation efficiency of TC decreased with an increase in the concentration of TC. Previous studies have reported that at higher concentrations of pollutants, more intermediates are produced, which enhances the adsorption competition between the pollutant and its degradation products (intermediates) on the catalyst surface [67]. Fig. 11d shows the pseudo-first order rate constant of 0.0112 min^{-1} at a dose of 25 mg/L, which however decreased to 0.0075 min^{-1} and 0.0052 min^{-1} at 50 mg/L and 75 mg/L, respectively. This could be attributed to the increase in the path length of photons entering the reaction system, thereby reducing the photons on the surface of the catalyst [68]. In addition, as tetracycline ions dominate the photocatalyst's active site, it causes a reduction in the number of hydroxyl radicals formed on the surface of the catalyst thereby decreasing the photocatalytic activity.

3.10. Degradation efficiency and kinetics of the degradation process by $BTiO_2$–ZnO, $BTiO_2$ and BZnO

To fully evaluate the photocatalytic degradation efficiency of TC by the studied photocatalysts, the adsorptive ability of each catalyst was assessed by first equilibrating the suspension in the dark for 30 min without light irradiation. Fig. 12(a–c) show the photocatalytic degradation graphs of TC by BZnO, $BTiO_2$ and $BTiO_2$–ZnO nanoparticles respectively under visible light illumination. The graphs are presented for the sake of comparison at the same experimental conditions of 50 mg/L concentration of TC at pH 7 and 100 mg/L of each catalyst was used. After 120 min of irradiation, 56, 58, and 63 % of TC was degraded with BZnO, $BTiO_2$ and $BTiO_2$–ZnO nanoparticles respectively (Fig. 11d). The rate of photocatalytic degradation of TC by BZnO, $BTiO_2$ and $BTiO_2$–ZnO nanoparticles are 0.0050 min^{-1}, 0.0056 min^{-1} and 0.0077 min^{-1} respectively Fig. 12e-g. Photocatalytic degradation efficiency of the synthesized photocatalysts on TC obtained in this current study and other related studies have been compared in Table 3. Variable amounts of the catalyst and TC concentration were used, which led to a considerable difference in the degradation efficiency. The improved photocatalytic activity of heterojunction composite of $BTiO_2$ and BZnO compared to the individual materials can be attributed to the transfer of electrons and holes, which takes place in $BTiO_2$ and BZnO as they possess different redox energy levels for their corresponding conduction and valence bands. Efficient charge separation increases the lifetime of the charge carriers and

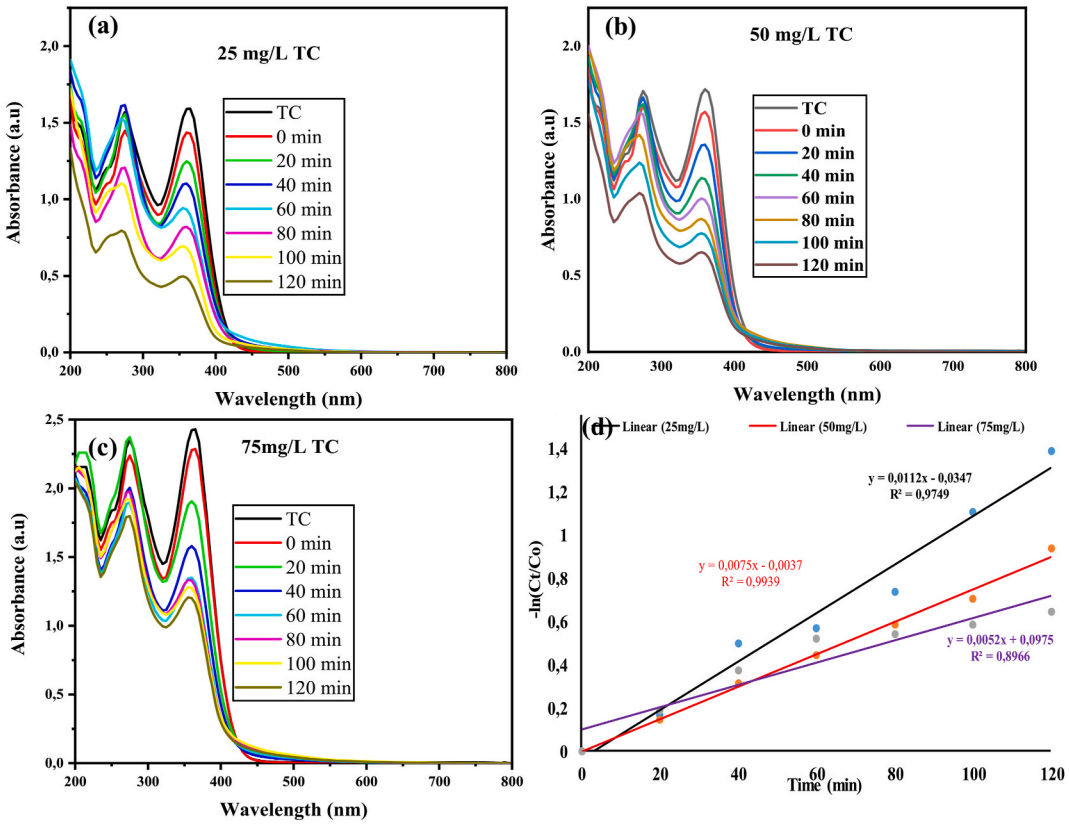

Fig. 11. Absorption spectra of TC showing its photodegradation by $BTiO_2$–ZnO nanocomposite at initial TC concentrations of (a) 25, (b) 50, and (c) 75 mg/L (d) The kinetics graph of the decomposition process.

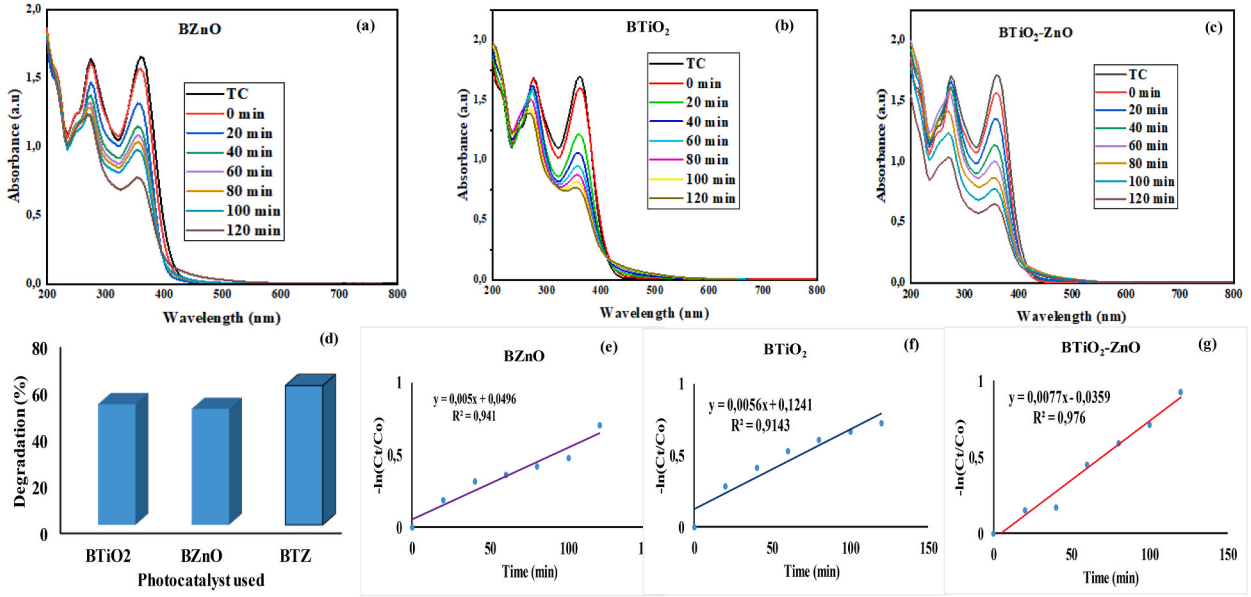

Fig. 12. (a–c) Absorption profile, (d) percentage degradation, and (e–g) kinetics graphs of BZnO, $BTiO_2$, and $BTiO_2$–ZnO, respectively and (100 mg/L photocatalyst, 50 mg/L TC and pH = 7.

Table 3
Comparison of TC degradation using the prepared $BTiO_2$–ZnO with other different TiO_2 or ZnO based advanced oxidation process catalysts earlier reported.

Nanomaterial	Catalyst (mg/L)	TC (mg/L)	pH	K (min^{-1})	Time (min)	Efficiency (%)	Ref.
TiO_2@ZnO	2500	10	11	0.0296	180	99.11	[74]
TiO2–ZnO/CS–Gr	500	20	4	–	180	97.2	[75]
ZnO/TiO_2 NBT	10	10	–	0.314	20	100	[76]
Black anatase-TiO_2	200	10	7.2	0.0045	270	66.2	[77]
ZnO/γ-Fe_2O_3	10	30	–	0.01321	160	83	[78]
TiO_2	1000	40	9.0	–	60	95	[53]
Ag/ZnO@Biochar	10	50	6.0	–	60	70.3	[79]
TiO_2	200	10	–	–	120	56.7	[77]
MWCNT/TiO_2	200	10	5.2	–	300	83	[80]
SDS/ZnO	20	40	7	–	150	49.0	[55]
TiO_2/activated carbon	1000	50	–	0.0029	75	100	[81]
$BTiO_2$–ZnO	100	50	7.0	0.0077	120	63	Present study
	125	50	7.0	–	120	74	

enhances the efficiency of the interfacial charge transfer to adsorbed substrates [69–71]. Increased oxygen vacancies on the surface of both BZnO and $BTiO_2$ in the heterostructure could have also contributed in the effective degradation efficiency of TC by acting as electron acceptors, thereby decreasing the surface recombination centers. Oxygen vacancies can also facilitate the adsorbed O_2 to capture photo-induced electrons, synchronously generating superoxide radical anions, thereby greatly enhancing the photocatalytic properties [72,73].

3.11. Photocatalytic mechanism

Fig. 13, illustrates the photocatalytic mechanism leading to the degradation of tetracycline using $BTiO_2$–ZnO heterojunction photocatalyst under visible light. The TiO_2–ZnO heterojunction photocatalyst formed electron-hole pairs upon irradiation by UV light with energy exceeding its band gap energy. The photoactive centre $BTiO_2$ and the electron trapping BZnO process contributed to the lowering of the rate of recombination of the electron-hole pairs that have strong reducing and oxidizing powers, respectively [82]. The efficient separation of photo-generated electrons is facilitated by the transfer of electrons from TiO_2 to ZnO and holes from ZnO to TiO_2. This minimizes charge carrier recombination during the electron transfer process, thereby improving the photocatalytic reaction. By generating a second electron trap site and facilitating electron transport from TiO_2 to ZnO, oxygen vacancies in the photocatalyst further increase the photocatalytic activity and lower the rate of electron-hole recombination. The oxygen vacancies also serve as a source of reactive species, such as hydroxyl and superoxide radicals, which aid the breakdown of tetracycline. Due to electrostatic attraction and van der Waals forces, the active antibiotic Tetracycline gets adsorbed onto the surface of the photocatalyst. The

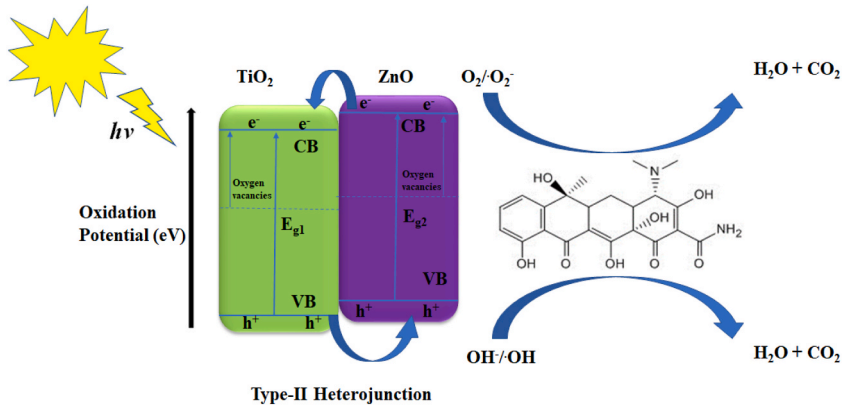

Fig. 13. Proposed mechanism for the photocatalytic degradation of Tetracycline with $BTiO_2$–ZnO.

adsorbed antibiotics are attacked by the hydroxyl radicals (•OH) produced when water molecules on the surface of the photocatalyst react with photogenerated holes (h^+). The •OH radicals attack the *C*–N–C fragment of TC, leading to the detachment of the *N*-methyl group [77]. The photocatalytic breakdown intermediates are further oxidized by hydroxyl radicals, which causes the tetracycline to completely mineralize into carbon dioxide, water, and inorganic ions by ring-opening processes.

4. Conclusion

The fabrication of a highly photocatalytically active surface defective heterojunction semiconductor system composed of TiO_2 and ZnO was successfully achieved through a two-step method. The method of synthesis facilitated the formation of oxygen vacancies through surface engineering. The $BTiO_2$–ZnO heterostructure was able to degrade 64 % of tetracycline, and it performed better as a photocatalyst than $BTiO_2$ and BZnO. The enhanced light absorption properties and improved charge separation of the photocatalyst due to the formation of heterojunction and oxygen vacancies might be attributed to the enhanced photocatalytic activity of $BTiO_2$–ZnO. The percentage degradation improved with increase in photocatalyst dosage, a decrease in the concentration of tetracycline concentration and a neutral condition. The study also confirmed that the solution pH plays a critical role in the degradation process. The outcomes of the study showed that the use of $BTiO_2$–ZnO heterostructure in the photocatalytic degradation of tetracycline in water may guide the development of novel future semiconductor photocatalysts in water treatment that utilizes cheap and effective multi-photocatalytic enhancement techniques.

Data availability statement

Data included in article/supp. Material/referenced in article.

CRediT authorship contribution statement

Lawrence Sawunyama: Writing – original draft, Methodology, Investigation, Formal analysis. **Opeyemi Oyewo:** Writing – review & editing, Supervision, Investigation. **Damian C. Onwudiwe:** Writing – review & editing, Supervision, Project administration, Funding acquisition, Conceptualization. **Seshibe S. Magkato:** Resources.

Declaration of competing interest

The authors declare that they have no known competing financial interests or personal relationships that could have appeared to influence the work reported in this paper.

Acknowledgement

The authors acknowledge the financial support from the North-West University, South Africa (1K02799).

Appendix A. Supplementary data

Supplementary data to this article can be found online at https://doi.org/10.1016/j.heliyon.2023.e21423.

References

[1] J.R. Rohr, C.B. Barrett, D.J. Civitello, M.E. Craft, B. Delius, G.A. DeLeo, P.J. Hudson, N. Jouanard, K.H. Nguyen, R.S. Ostfeld, J.V. Remais, G. Riveau, S. H. Sokolow, D. Tilman, Emerging human infectious diseases and the links to global food production, Nat. Sustain. 2 (2019) 445–456.
[2] R. Daghrir, P. Drogui, Tetracycline antibiotics in the environment: a review, Environ. Chem. Lett. 11 (2013) 209–227.
[3] J. Lyu, L. Yang, L. Zhang, B. Ye, L. Wang, Antibiotics in soil and water in China-a systematic review and source analysis, Environ. Pollut. 266 (2020), 115147.
[4] L. Andronic, A.J.F.i.C. Enesca, Black TiO2 synthesis by chemical reduction methods for photocatalysis applications 8 (2020), 565489.
[5] M. Bilal, S. Mehmood, T. Rasheed, H.M.N. Iqbal, Antibiotics traces in the aquatic environment: persistence and adverse environmental impact, Current Opinion in Environ. Sci. Health 13 (2020) 68–74.
[6] S.I. Polianciuc, A.E. Gurzau, B. Kiss, M.G. Stefan, F. Loghin, Antibiotics in the environment: causes and consequences, Med Pharm Rep 93 (2020) 231–240.
[7] Y. Amangelsin, Y. Semenova, M. Dadar, M. Aljofan, G. Bjørklund, The impact of tetracycline pollution on the aquatic environment and removal strategies, Antibiotics 12 (2023) 440.
[8] V. Faus-Matoses, I. Faus-Matoses, E. Ruiz-Bell, V.J. Faus-Llácer, Severe tetracycline dental discoloration: restoration with conventional feldspathic ceramic veneers. A clinical report, J. Clinic. Experimen. Dentist. 9 (2017) e1379.
[9] B.L. Phoon, C.C. Ong, M.S. Mohamed Saheed, P.L. Show, J.S. Chang, T.C. Ling, S.S. Lam, J.C. Juan, Conventional and emerging technologies for removal of antibiotics from wastewater, J. Hazard Mater. 400 (2020), 122961.
[10] OECD, Pharmaceutical residues in freshwater: hazards and policy responses, in: Hazards and Policy Responses, OECD Publishing, Paris, 2019.
[11] T.O. Ajiboye, L. Saunyama, M. Ravele, A.A. Rasheed-Adeleke, N. Seheri, D.C. Onwudiwe, S.D. Mhlanga, Synthesis approaches to ceramic membranes, their composites, and application in the removal of tetracycline from water, Environ. Adv. (2023), 100371.
[12] T. Heberer, D.J.P.i.t.E.S, Feldmann, Fate, Effects, Risks, Removal of Pharmaceutical Residues from Contaminated Raw Water Sources by Membrane Filtration, 2008, pp. 427–453.
[13] W.-Y. Li, Q. Wang, Q.-F. Xiao, B.-Z. Dong, Removal of tetracycline and oxytetracycline in water by a reverse osmosis membrane, in: 3rd International Conference on Bioinformatics and Biomedical Engineering, IEEE, 2009, pp. 1–4, 2009.
[14] P.M. Nguyen, M. Afzal, I. Ullah, N. Shahid, M. Baqar, M. Arslan, Removal of pharmaceuticals and personal care products using constructed wetlands: effective plant-bacteria synergism may enhance degradation efficiency, Environ. Sci. Pollut. Res. Int. 26 (2019) 21109–21126.
[15] L. Paredes, S. Murgolo, H. Dzinun, M.H.D. Othman, A.F. Ismail, M. Carballa, G. Mascolo, Application of immobilized TiO2 on PVDF dual layer hollow fibre membrane to improve the photocatalytic removal of pharmaceuticals in different water matrices, Appl. Catal. B Environ. 240 (2019) 9–18.
[16] J.B. Ouyang, L.M. Zhou, Z.R. Liu, J.Y.Y. Heng, W.Q. Chen, Biomass-derived activated carbons for the removal of pharmaceutical mircopollutants from wastewater: a review, Separ. Purif. Technol. 253 (2020), 117536.
[17] L. Sawunyama, O.A. Oyewo, N. Seheri, S.A. Onjefu, D.C. Onwudiwe, Metal oxide functionalized ceramic membranes for the removal of pharmaceuticals in wastewater, Surface. Interfac. (2023), 102787.
[18] A. Saravanan, V. Deivayanai, P.S. Kumar, G. Rangasamy, R. Hemavathy, T. Harshana, N. Gayathri, A. Krishnapandi, A detailed review on advanced oxidation process in treatment of wastewater: mechanism, challenges and future outlook, Chemosphere (2022), 136524.
[19] R.A. Goncalves, R.P. Toledo, N. Joshi, O.M. Berengue, Green synthesis and applications of ZnO and TiO(2) nanostructures, Molecules 26 (2021) 2236.
[20] X. Cao, Y. Chen, J. Tang, H. Zhang, X. Tang, Mechanistic study of nitrogen-modified titanium dioxide nanoparticles for enhancing the degradation of organic dyes and antibacterial properties under visible-light irradiation, Mater. Today Commun. (2023), 106166.
[21] B. Han, W. Wei, M. Li, K. Sun, Y.H. Hu, A thermo-photo hybrid process for steam reforming of methane: highly efficient visible light photocatalysis, Chem. Commun. 55 (2019) 7816–7819.
[22] I. Arora, H. Chawla, A. Chandra, S. Sagadevan, S. Garg, Advances in the strategies for enhancing the photocatalytic activity of TiO2: conversion from UV-light active to visible-light active photocatalyst, Inorg. Chem. Commun. 143 (2022), 109700.
[23] N. Apostolescu, R.E.T. Farmus, M. Harja, M.A. Vizitiu, C. Cernatescu, C. Cobzaru, G.A. Apostolescu, Photocatalytic removal of antibiotics from wastewater using the CeO2/ZnO heterojunction, Materials 16 (2023) 850.
[24] M.M. Ali, M.J. Haque, M.H. Kabir, M.A. Kaiyum, M. Rahman, Nano synthesis of ZnO–TiO2 composites by sol-gel method and evaluation of their antibacterial, optical and photocatalytic activities, Results in Materials 11 (2021), 100199.
[25] T.S. Rajaraman, V.G. Gandhi, V.H. Nguyen, S.P. Parikh, Aluminium foil-assisted NaBH4 reduced TiO2 with surface defects for photocatalytic degradation of toxic fuchsin basic dye, Appl. Nanosci. (2022) 1–20.
[26] S. Sunaryono, S.N. Halizah, S. Zulaikah, H. Susanto, N. Mufti, A. Taufiq, Contribution of ZnO/TiO2 nanocomposite particles towards bacterial growth inhibition, in: AIP Conference Proceedings, AIP Publishing LLC, 2021, 030013.
[27] G. Rajakumar, A.A. Rahuman, S.M. Roopan, V.G. Khanna, G. Elango, C. Kamaraj, A.A. Zahir, K. Velayutham, Fungus-mediated biosynthesis and characterization of TiO2 nanoparticles and their activity against pathogenic bacteria, Spectrochim. Acta Mol. Biomol. Spectrosc. 91 (2012) 23–29.
[28] L. Chougala, M. Yatnatti, R. Linganagoudar, R. Kamble, J. Kadadevarmath, A Simple Approach on Synthesis of TiO2 Nanoparticles and its Application in Dye Sensitized Solar Cells, 2017.
[29] S.S. Al-Taweel, H.R. Saud, New route for synthesis of pure anatase TiO2 nanoparticles via utrasound-assisted sol-gel method, J. Chem. Pharmaceut. Res. 8 (2016) 620–626.
[30] P. Praveen, G. Viruthagiri, S. Mugundan, N. Shanmugam, Structural, optical and morphological analyses of pristine titanium di-oxide nanoparticles–synthesized via sol-gel route, Spectrochim. Acta Mol. Biomol. Spectrosc. 117 (2014) 622–629.
[31] M.M. Ba-Abbad, A.A.H. Kadhum, A.B. Mohamad, M.S. Takriff, K. Sopian, Synthesis and catalytic activity of TiO2 nanoparticles for photochemical oxidation of concentrated chlorophenols under direct solar radiation, Int. J. Electrochem. Sci. 7 (2012) 4871–4888.
[32] A.A. Sharwani, K.B. Narayanan, M.E. Khan, S.S. Han, Photocatalytic degradation activity of goji berry extract synthesized silver-loaded mesoporous zinc oxide (Ag@ZnO) nanocomposites under simulated solar light irradiation, Sci. Rep. 12 (2022), 10017.
[33] T.L. Valerio, G.A.R. Maia, L.F. Gonçalves, A. Viomar, E.d.P. Banczek, P.R.P. Rodrigues, Study of the Nb 2 O 5 insertion in ZnO to dye-sensitized solar cells, Mater. Res. 22 (2019).
[34] A.A. Menazea, N.S. Awwad, Antibacterial activity of TiO2 doped ZnO composite synthesized via laser ablation route for antimicrobial application, J. Materi. Res. Technol.-JMR&T 9 (2020) 9434–9441.
[35] S.P. Rajendran, K. Sengodan, Synthesis and characterization of zinc oxide and iron oxide nanoparticles using Sesbania grandiflora leaf extract as reducing agent, J. Nanosci. (2017) 2017.
[36] H.M. Mousa, J.F. Alenezi, I.M.A. Mohamed, A.S. Yasin, A.F.M. Hashem, A. Abdal-hay, Synthesis of TiO2@ZnO heterojunction for dye photodegradation and wastewater treatment, J. Alloys Compd. 886 (2021), 161169.
[37] W. Li, R. Liang, A. Hu, Z. Huang, Y.N.J.R.a. Zhou, Generation of oxygen vacancies in visible light activated one-dimensional iodine TiO 2 photocatalysts 4 (2014) 36959–36966.
[38] L.L. Zhang, Z.P. Xing, H. Zhang, Z.Z. Li, X.Y. Wu, X.D. Zhang, Y. Zhang, W. Zhou, High thermostable ordered mesoporous SiO2-TiO2 coated circulating-bed biofilm reactor for unpredictable photocatalytic and biocatalytic performance, Appl. Catal. B Environ. 180 (2016) 521–529.
[39] E.M. Al-Khalqi, M.A. Abdul Hamid, N.H. Al-Hardan, L.K. Keng, Highly sensitive magnesium-doped ZnO nanorod pH sensors based on electrolyte–insulator–semiconductor (EIS) Sensors, Sensors 21 (2021) 2110.
[40] X. Cao, A. Huang, C. Liang, H.C. Chen, T. Han, R. Lin, Q. Peng, Z. Zhuang, R. Shen, H.M. Chen, Y. Yu, C. Chen, Y. Li, Engineering lattice disorder on a photocatalyst: photochromic BiOBr nanosheets enhance activation of aromatic C-H bonds via water oxidation, J. Am. Chem. Soc. 144 (2022) 3386–3397.
[41] Y. Hu, Y. Pan, Z. Wang, T. Lin, Y. Gao, B. Luo, H. Hu, F. Fan, G. Liu, L. Wang, Lattice distortion induced internal electric field in TiO2 photoelectrode for efficient charge separation and transfer, Nat. Commun. 11 (2020) 2129.

[42] N. Siregar, Motlan, J.H. Panggabean, M. Sirait, J. Rajagukguk, N.S. Gultom, F.K. Sabir, Fabrication of dye-sensitized solar cells (DSSC) using Mg-doped ZnO as photoanode and extract of rose myrtle (Rhodomyrtus tomentosa) as natural dye, Int. J. Photoenergy 2021 (2021) 1–7.
[43] I. Sutapa, A. Wahid Wahab, P. Taba, N. Nafie, Dislocation, crystallite size distribution and lattice strain of magnesium oxide nanoparticles, in: Journal of Physics: Conference Series, IOP Publishing, 2018, 012021.
[44] M.M. Momeni, M. Taghinejad, Y. Ghayeb, R. Bagheri, Z. Song, Preparation of various boron-doped TiO 2 nanostructures by in situ anodizing method and investigation of their photoelectrochemical and photocathodic protection properties, J. Iran. Chem. Soc. 16 (2019) 1839–1851.
[45] Y. Abdissa, K. Siraj, G. Selale, Effect of Mg2+, Ca2+ and Sr2+ ions doping on the band gap energy of ZnO nanoparticle, Juniper Online J. Mater. Sci. 3 (2018) 1–6.
[46] Q. Wang, X. Qian, H. Xu, G. He, H. Chen, Enriched surface oxygen vacancies of Bi2WO6/NH2-MIL-68 (In) Z-scheme heterojunction with boosted visible-light photocatalytic degradation for levofloxacin: performance, degradation pathway and mechanism insight, Separ. Purif. Technol. 306 (2023), 122577.
[47] J. Hidalgo-Jimenez, Q. Wang, K. Edalati, J.M. Cubero-Sesin, H. Razavi-Khosroshahi, Y. Ikoma, D. Gutierrez-Fallas, F.A. Dittel-Meza, J.C. Rodriguez-Rufino, M. Fuji, Z. Horita, Phase transformations, vacancy formation and variations of optical and photocatalytic properties in TiO2-ZnO composites by high-pressure torsion, Int. J. Plast. 124 (2020) 170–185.
[48] H.M. Mousa, J.F. Alenezi, I.M. Mohamed, A.S. Yasin, A.-F.M. Hashem, A. Abdal-Hay, Synthesis of TiO2@ ZnO heterojunction for dye photodegradation and wastewater treatment, J. Alloys Compd. 886 (2021), 161169.
[49] F. Pellegrino, L. Pellutie, F. Sordello, C. Minero, E. Ortel, V.D. Hodoroaba, V. Maurino, Influence of agglomeration and aggregation on the photocatalytic activity of TiO2 nanoparticles, Appl. Catal. B Environ. 216 (2017) 80–87.
[50] Y. Liao, C. Xie, Y. Liu, H. Chen, H. Li, J. Wu, Comparison on photocatalytic degradation of gaseous formaldehyde by TiO2, ZnO and their composite, Ceram. Int. 38 (2012) 4437–4444.
[51] F. Saadati, N. Keramati, M.M. Ghazi, Influence of parameters on the photocatalytic degradation of tetracycline in wastewater: a review, Crit. Rev. Environ. Sci. Technol. 46 (2016) 757–782.
[52] K. Divakaran, A. Baishnisha, V. Balakumar, K.N. Perumal, C. Meenakshi, R.S. Kannan, Photocatalytic degradation of tetracycline under visible light using TiO2@sulfur doped carbon nitride nanocomposite synthesized via in-situ method, J. Environ. Chem. Eng. 9 (2021), 105560.
[53] X.D. Zhu, Y.J. Wang, R.J. Sun, D.M. Zhou, Photocatalytic degradation of tetracycline in aqueous solution by nanosized TiO2, Chemosphere 92 (2013) 925–932.
[54] G.H. Safari, M. Hoseini, M. Seyedsalehi, H. Kamani, J. Jaafari, A.H. Mahvi, Photocatalytic degradation of tetracycline using nanosized titanium dioxide in aqueous solution, Int. J. Environ. Sci. Technol. 12 (2015) 603–616.
[55] K. Jia, G. Liu, D.N. Lang, S.F. Chen, C. Yang, R.L. Wu, W. Wang, J.D. Wang, Degradation of tetracycline by visible light over ZnO nanophotocatalyst, J. Taiwan Inst. Chem. Eng. 136 (2022), 104422.
[56] C. Song, H.Y. Liu, S. Guo, S.G. Wang, Photolysis mechanisms of tetracycline under UV irradiation in simulated aquatic environment surrounding limestone, Chemosphere 244 (2020), 125582.
[57] K. Chand, C. Jiao, M.N. Lakhan, A.H. Shah, V. Kumar, D.E. Fouad, M.B. Chandio, A.A. Maitlo, M. Ahmed, D. Cao, Green synthesis, characterization and photocatalytic activity of silver nanoparticles synthesized with Nigella Sativa seed extract, Chem. Phys. Lett. 763 (2021), 138218.
[58] Y. Mbenga, M.S. Mthana, D.M. Mthiyane, O.E. Ogunjinmi, M. Singh, D.C. Onwudiwe, Facile biosynthesis of CaO nanoparticles using extract of Tulbaghia violacea and evaluation of their antibacterial and cytotoxicity activity, Inorg. Chem. Commun. 151 (2023), 110581.
[59] S. Raja, V. Ramesh, V. Thivaharan, Green biosynthesis of silver nanoparticles using Calliandra haematocephala leaf extract, their antibacterial activity and hydrogen peroxide sensing capability, Arab. J. Chem. 10 (2017) 253–261.
[60] Z. Li, L. Schulz, C. Ackley, N. Fenske, Adsorption of tetracycline on kaolinite with pH-dependent surface charges, J. Colloid Interface Sci. 351 (2010) 254–260.
[61] J.D. Clogston, A.K. Patri, Zeta potential measurement, Methods Mol. Biol. 697 (2011) 63–70.
[62] L. William, IV, I. Kostedt, A.A. Ismail, D.W. Mazyck, Impact of heat treatment and composition of ZnO− TiO2 nanoparticles for photocatalytic oxidation of an azo dye, Ind. Eng. Chem. Res. 47 (2008) 1483–1487.
[63] S. Jiao, S. Zheng, D. Yin, L. Wang, L. Chen, Aqueous photolysis of tetracycline and toxicity of photolytic products to luminescent bacteria, Chemosphere 73 (2008) 377–382.
[64] J.J. López-Peñalver, M. Sánchez-Polo, C.V. Gómez-Pacheco, J.J.J.o.C.T, Rivera Utrilla, Biotechnology, Photodegradation of Tetracyclines in Aqueous Solution by Using UV and UV/H2O2 Oxidation Processes, vol. 85, 2010, pp. 1325–1333.
[65] Y.M. Hunge, A. Yadav, S.-W. Kang, H. Kim, Photocatalytic degradation of tetracycline antibiotics using hydrothermally synthesized two-dimensional molybdenum disulfide/titanium dioxide composites, J. Colloid Interface Sci. 606 (2022) 454–463.
[66] M.P. Ravele, O.A. Oyewo, S. Ramaila, L. Mavuru, D.C. Onwudiwe, Photocatalytic degradation of tetracycline in aqueous solution using copper sulfide nanoparticles, Catalysts 11 (2021) 1238.
[67] F. Chen, Q. Yang, Y. Zhong, H. An, J. Zhao, T. Xie, Q. Xu, X. Li, D. Wang, G. Zeng, Photo-reduction of bromate in drinking water by metallic Ag and reduced graphene oxide (RGO) jointly modified BiVO4 under visible light irradiation, Water Res. 101 (2016) 555–563.
[68] X. Wang, G. Zhu, C. Wang, Y. Niu, Effective degradation of tetracycline by organic-inorganic hybrid materials induced by triethylenediamine, Environ. Res. 198 (2021), 111253.
[69] D.L. Liao, C.A. Badour, B.Q. Liao, Preparation of nanosized TiO2/ZnO composite catalyst and its photocatalytic activity for degradation of methyl orange, J. Photochem. Photobiol. Chem. 194 (2008) 11–19.
[70] R. Qin, F.M. Meng, M.W. Khan, B. Yu, H.J. Li, Z.H. Fan, J.F. Gong, Fabrication and enhanced photocatalytic property of TiO2-ZnO composite photocatalysts, Mater. Lett. 240 (2019) 84–87.
[71] M. Tian, M. Mahjouri-Samani, G. Eres, R. Sachan, M. Yoon, M.F. Chisholm, K. Wang, A.A. Puretzky, C.M. Rouleau, D.B. Geohegan, G. Duscher, Structure and formation mechanism of black TiO2 nanoparticles, ACS Nano 9 (2015) 10482–10488.
[72] C. Wang, D. Wu, P.F. Wang, Y.H. Ao, J. Hou, J. Qian, Effect of oxygen vacancy on enhanced photocatalytic activity of reduced ZnO nanorod arrays, Appl. Surf. Sci. 325 (2015) 112–116.
[73] S.G. Ullattil, S.B. Narendranath, S.C. Pillai, P. Periyat, Black TiO2 nanomaterials: a review of recent advances, Chem. Eng. J. 343 (2018) 708–736.
[74] S.Z. Heris, M. Etemadi, S. Mousavi, M. Mohammadpourfard, B. Ramavandi, Preparation and characterizations of TiO2/ZnO nanohybrid and its application in photocatalytic degradation of tetracycline in wastewater, J. Photochem. Photobiol. A 443 (2023), 114893.
[75] H. Asadzadeh Patehkhor, M. Fattahi, M. Khosravi-Nikou, Synthesis and characterization of ternary chitosan–TiO2–ZnO over graphene for photocatalytic degradation of tetracycline from pharmaceutical wastewater, Sci. Rep. 11 (2021) 1–17.
[76] Q. Jiang, Z. Han, Y. Qian, Y. Yuan, Y. Ren, M. Wang, Z. Cheng, Enhanced visible-light photocatalytic performance of ZIF-8-derived ZnO/TiO2 nano-burst-tube by solvothermal system adjustment, J. Water Proc. Eng. 47 (2022), 102768.
[77] S. Wu, X. Li, Y. Tian, Y. Lin, Y.H. Hu, Excellent photocatalytic degradation of tetracycline over black anatase-TiO2 under visible light, Chem. Eng. J. 406 (2021), 126747.
[78] P. Semeraro, S. Bettini, S. Sawalha, S. Pal, A. Licciulli, F. Marzo, N. Lovergine, L. Valli, G. Giancane, Photocatalytic degradation of tetracycline by ZnO/γ-Fe2O3 paramagnetic nanocomposite material, Nanomaterials 10 (2020) 1458.
[79] M. Hosny, M. Fawzy, A.S. Eltaweil, Green synthesis of bimetallic Ag/ZnO@ Biohar nanocomposite for photocatalytic degradation of tetracycline, antibacterial and antioxidant activities, Sci. Rep. 12 (2022) 7316.
[80] P. Wang, P.-S. Yap, T.-T. Lim, C–N–S tridoped TiO2 for photocatalytic degradation of tetracycline under visible-light irradiation, Appl. Catal. Gen. 399 (2011) 252–261.
[81] A.C. Martins, A.L. Cazetta, O. Pezoti, J.R. Souza, T. Zhang, E.J. Pilau, T. Asefa, V.C. Almeida, Sol-gel synthesis of new TiO2/activated carbon photocatalyst and its application for degradation of tetracycline, Ceram. Int. 43 (2017) 4411–4418.
[82] A. Haghighizadeh, A. Aghababai Beni, M. Haghmohammadi, M.S.S. Adel, S. Farshad, Green synthesis of ZnO-TiO2 nano-photocatalyst doped with Fe (III) ions using bitter olive extract to treat textile wastewater containing reactive dyes, Water, air, & Soil Pollution 234 (2023) 1–17.